Supporting Information

Experimental and CFD investigation of inert bed materials effects in a high-temperature conical cavity-type reactor for continuous solar-driven steam gasification of biomass

Houssame Boujjat[1,2], Sylvain Rodat[3], Srirat Chuayboon[3], Stéphane Abanades[3*]

[1]*CEA-LITEN Solar and Thermodynamic Systems Laboratory (L2ST), F-38054 Grenoble, France*

[2]*Univ. Grenoble Alpes, F-38000 Grenoble, France*

[3]*Processes, Materials and Solar Energy Laboratory, PROMES-CNRS, 7 Rue du Four Solaire, 66120 Font-Romeu, France*

*Corresponding author: stephane.abanades@promes.cnrs.fr

1. Experimental set up

1.1 Solar facility

The solar reactor is installed and operated at the focus of a vertical-axis parabolic concentrator located at the 6th floor of the CNRS-PROMES building (Figure.SI 1). All along the experiments, a sun tracking heliostat is used to reflect the solar rays towards the 2 m-diameter face down parabolic mirror that in turn concentrates the radiations towards the reactor. The reactor aperture is settled at the focal point of the solar concentrator where the flux density exceeds 10 MW/m^2 (for a DNI of 1 kW/m^2) with a Gaussian distribution.

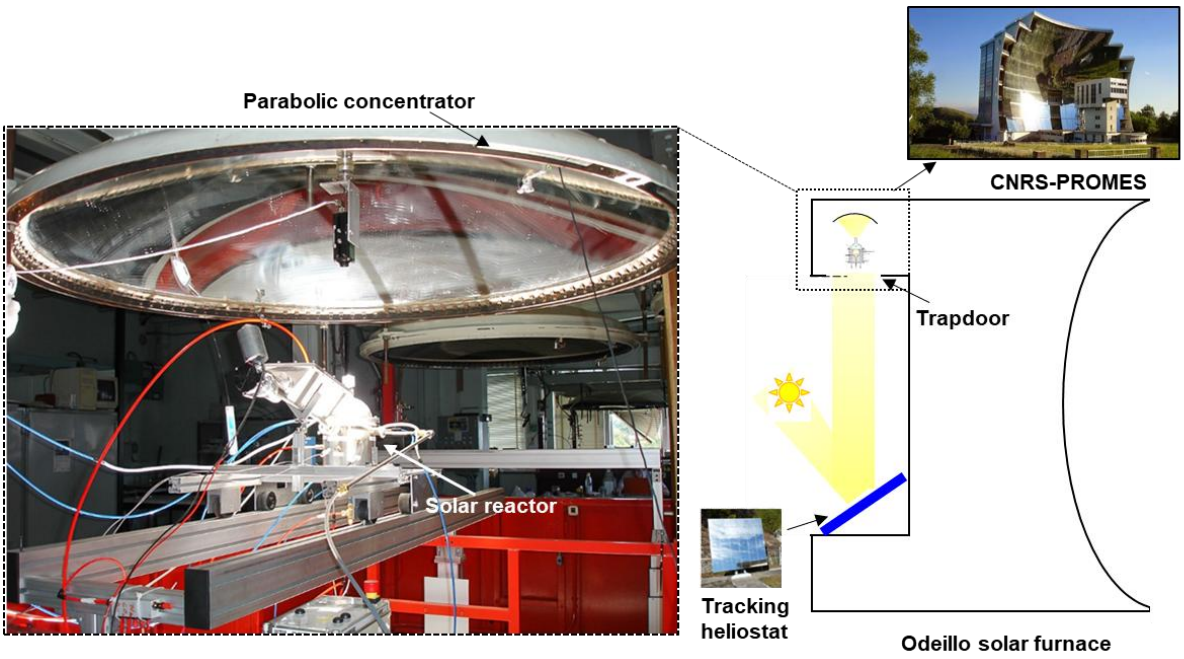

Figure SI 1. Solar facilities and reactor at the focus of the solar concentrator

1.2 Bed materials

An illustration of the three hydrodynamic configurations i.e. dilute spouted bed (empty cavity), spouted bed and packed bed is shown in Figure.SI 2

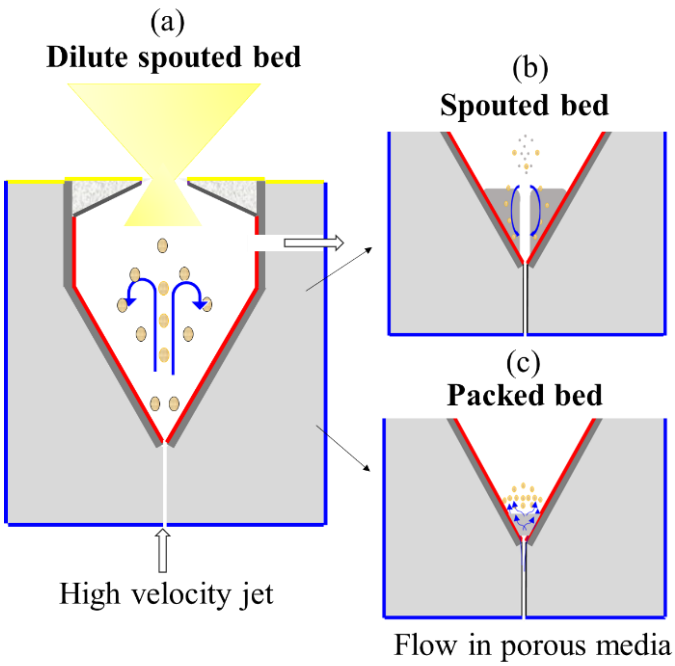

Figure SI 2. Illustration of particles effects on the gasification process: (a) Dilute spouted bed (volume fraction of the wood particles less than 1%), (b) Spouted bed (with inert powders), (c) Packed bed (inert porous particle bed at the bottom)

2. Model development

2.1 Geometry, mesh and boundary conditions

Two thermal CFD models were developed. The first one simulates the fluid flow through the porous packed bed medium. The second one uses the Eulerian-Eulerian model to simulate the directly irradiated spouted bed particles. Figure.SI 3 shows the global 2D geometry and Boundary Conditions (BCs).

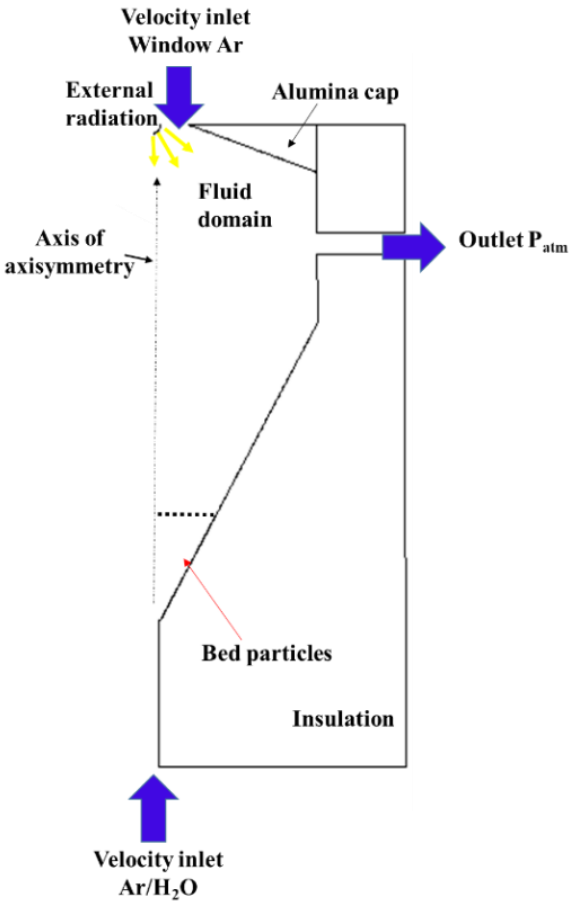

Figure SI 3. 2D Axisymmetric geometry of the reactor

Radiative heat losses from the reactor alumina cap and upper insulation were considered, assuming radiation exchange with an external black body at 25°C. The reactor external borders were water-cooled and maintained at 25°C. The radiative source that represents the incoming concentrated solar power is a semi-transparent surface allowing reradiation outside of the reactor and is specified in terms of an incident radiant heat flux (W/m^2) assumed specular. The internal reactor walls were considered as diffuse with constant emissivity ($\varepsilon_{cavity\ wall}$=0.7, $\varepsilon_{Alumina\ cap\ wall}$=0.8). A velocity inlet condition of 0.1 m/s (2 Nl/min) was set for the upper Ar window inlet and of 3 m/s (0.2 Nl/min of Ar and 0.2 g/min of steam, 36 wt. % of steam) for the bottom spouting gas inlet. All the gases were injected at an initial temperature of 25°C. The outlet pressure was equal to the atmospheric pressure (around 860 hPa). To simulate the gasification reactions, a volumetric heat sink ($S_{rxn}=F_{biomass}.\Delta H_g/V_{fluid}$) was applied to the fluid region. The enthalpy of the steam gasification reaction for the considered biomass was ΔH_g = 0.84 MJ/mol. A no-slip boundary condition at the reactor walls was used for the gas phase.

- The packed bed was simulated using the porous zone technique to model both the fluid flow and heat transfer through the packed bed considered as a porous medium (characterized by a fixed porosity). The

top surface of the bed can potentially interact with discrete phase particles (such as char particles) via rebound/reflect BC.

- The spouted particles were modelled by the Eulerian approach. The interaction of the particles with the cavity walls was modelled by the Johnson and Jackson (Johnson and Jackson, 2006) wall boundary condition. This wall boundary condition involves two important parameters: the specularity coefficient, Φ, that specifies the shear condition at the walls, and the particle–wall restitution coefficient, e_w, that describes the dissipation of the solids kinetic energy with the wall by collisions. In this work, Φ and e_w were assumed both equal to 0.9.

A grid of 10521 quadrilateral and triangular elements was generated. The average mesh skewness was $8.2x10^{-2}$ with a standard deviation of $9.2x10^{-2}$. The average orthogonal quality was 0.95 with a standard deviation of $6.7x10^{-2}$. Grid resolution is very important to increase model accuracy. A preliminary sensitivity study of simulation outputs to the reactor mesh allowed choosing the optimal cell size inside the cavity (gas phase/reaction zone) to accurately solve the gradients in the spout (central) region of the reactor where sharp changes in terms of velocity, temperature and species molar fraction occur (Boujjat et al., 2019). A mesh size of around 0.8 mm offered a good compromise between precision and computational time. Therefore, the grid size in the inlet tube was set to 0.15 mm and it was increased smoothly (with a growth ratio of 1.2) to 0.8 mm inside the conical cavity. For fluidized bed gasifiers, a cell size of about 12 times the average particle size was able to effectively capture the gas-particles flow hydrodynamics (Ismail et al., 2018; Gelderbloom et al., 2009; Wang, 2008). In this study, the spouted bed particles size was in the range of 125µm to 300µm; therefore, the generated mesh met also this criterion.

2.2 Governing equations

Prior to the CFD simulations, and to assess the impact of turbulence in the current flow configuration, the Reynolds ($Re=\rho.V.L/\mu$) number was calculated. Assuming a gas mixture composed of 64 wt. % of argon and 36 wt. % of steam in the injection tube (calculated from the high temperature experimental flow rates), a characteristic velocity of 10 m/s at the inlet of the conical cavity (exit of injection tube), a characteristic flow length scale of 2 mm (which is the diameter of the injection tube) and a characteristic temperature of 700°C, a Re number of 136 was calculated. This value is below 2300, which is the critical Re number in pipes, and below 300-450, which is the critical Re number in confined coaxial jets (Gore and Crowe, 1988). The dissipative effects are expected to be more pronounced at the near hot wall regions where gas density is lower and viscosity is higher. The reactor small dimensions, small flow rates and high temperature are the three important factors that result in the low Reynolds numbers. This substantially limits the impact of turbulence on heat/mass transfer and mixing. Accordingly, a laminar solver was selected for all the cases for solving the conservation equations.

Simulations were performed with and without the injection of discrete phase char particles for the empty and packed-bed configurations. Table.SI 1 lists the model equations.

Table SI 1. Governing equations (empty and packed-bed configurations)

Continuity equation	$\frac{\partial \rho}{\partial t} + \nabla.(\rho v)$=0	(1)
Navier-Stokes equation	$\frac{\partial \rho v}{\partial t} + \nabla.\left(\rho v(v)\right) = -\nabla p + \nabla.\left(\overline{\overline{\tau_g}}\right) + \rho g + \mathrm{S}$	(2)
	With $\overline{\overline{\tau}} = \mu_g[(\nabla.v + \nabla v^T)] - \frac{2}{3}\nabla v.\bar{\bar{I}}$	(3)
Energy equation	$\frac{\partial(\epsilon\rho_g E_g + (1-\epsilon)\rho_s E_s)}{\partial t} + \nabla.\left(v\left(\rho_g E_g + p\right)\right) = \nabla.\left((\epsilon.\lambda_g -\right.$ $\left.(1-\epsilon).\lambda_s).\nabla T - \sum h_j j_j\right) + S_{rad,g} + S_{rxn}$	(4)
Gas species transport	$\frac{\partial \rho Y_i}{\partial t} + \nabla.(\rho v Y_i) = \nabla.(\rho D_{i,m} \nabla Y_i)$	(5)
Radiation equation	$\nabla.(I.s) + (a_g + a_{char}).I(r,s) = \frac{a_g.\sigma_{rad}T^4}{\pi} + E_{char} +$ $\frac{\sigma_{char}}{4.\pi}.\int_0^{4.\pi} I(r,s).\Phi_{isotropic}(s,s')d\Omega'$	(6)
DPM char particles	$\frac{dv_{char}}{dt} = F_D(v - v_{char}) + \frac{g.(\rho_{char}-\rho)}{\rho_{char}}$	(7)
	$m_{char}c_{char}\frac{dT_{char}}{dt} =$ $h'A_{char}(T_\infty - T_{char}) + \sigma_{rad}A_{char}\varepsilon_{char}\left({\theta_R}^4 - {T_{char}}^4\right)$	(8)

where S (in Eq.2) is the momentum sink due to the pressure loss across the randomly packed-bed particles. This pressure loss is generally expressed by Eq.9:

$$S_i = -\frac{\mu}{\alpha}.v_i - \frac{1}{2}.C_i\rho\,|v_i|.v_i \quad (9)$$

Where α is the permeability of the packed-bed and C_i the coefficient of inertial resistance, the latter parameter can be neglected in case of low Re numbers. Hence, only the first term of this equation was considered and the permeability of the medium was estimated according to the Kozeny-Carman equation with $\alpha \sim \{{180.\epsilon^2}/{d^2{}_s.(1-\epsilon)^3}\}$, ε the fluid porosity assumed equal to 0.37 (ε=0 for the empty configuration), d_s is the particles average diameter (considered here equal to 3mm). E_g and E_s are the gas and the packed particles total energy. λ_g and λ_s are the thermal conductivities of the gas and of the packed particles (Al_2O_3).

For the spouted-bed configuration, the equations in Table.SI 2 were solved for both the gas and the solid phases. The Eulerian-Eulerian treatment used for modelling the solid/gas system solves conservation laws written for both solid and gas phases at each cell of the CFD domain. Each cell is characterized by a phasic volume fraction α representing the space occupied by the corresponding phase. This model does not allow a direct calculation of the properties of each solid particle in the domain, but rather provides information on the effective property (such as temperature, velocity, etc.)

of the solids at a cell as calculated by the conservation equations. Each cell contains a given number of particles that defines the solid volume fraction.

Table SI 2. Governing equations (spouted particles configuration)

Continuity equation	Fluid phase $\frac{\partial \alpha_g \rho_g}{\partial t} + \nabla.\left(\alpha_g \rho_g v_g\right) = 0$	(10)
	Solid phase $\frac{\partial \alpha_s \rho_s}{\partial t} + \nabla.\left(\alpha_s \rho_s v_s\right) = 0$	(11)
	$\alpha_s + \alpha_g = 1$	(12)
Momentum equations	Fluid phase $\frac{\partial \alpha_g \rho_g \vec{v}_g}{\partial t} + \nabla.\left(\alpha_g \rho_g \vec{v}_g.\vec{v}_g\right) = -\alpha_g.\nabla p + \nabla.\bar{\bar{\tau}}_g + \alpha_g \rho_g \vec{g} + \beta(\vec{v}_s - \vec{v}_g)$ (13)	
	Solid phase $\frac{\partial \alpha_s \rho_s \vec{v}_s}{\partial t} + \nabla.\left(\alpha_s \rho_s \vec{v}_s.\vec{v}_s\right) = -\alpha_s.\nabla p - \nabla p_s + \nabla.\bar{\bar{\tau}}_s + \alpha_s \rho_s \vec{g} + \beta(\vec{v}_g - \vec{v}_s)$ (14)	
Granular temperature equation	$\frac{3}{2}\left[\frac{\partial \alpha_s \rho_s \theta_s}{\partial t} + \nabla.\left(\alpha_s \rho_s \vec{v}_s.\theta_s\right)\right] = \left(-p_s \bar{\bar{I}}. + \bar{\bar{\tau}}_s\right):\nabla \vec{v}_s + \nabla.\left(k_{\theta_s}.\nabla\,\theta_s\right) - \gamma_{\theta_s} + \varphi_{gs}$ (15)	
Gas species transport	$\frac{\partial \alpha_g \rho_g Y_{i,g}}{\partial t} + \nabla.\left(\alpha_g \rho_g \vec{v}_g.Y_{i,g}\right) = \nabla.\left(\nabla \alpha_g \rho_g Y_{i,g}\right)$	(16)
Energy conservation equation	Fluid phase $\frac{\partial \alpha_g \rho_g E_g}{\partial t} + \nabla.\left(\alpha_g \rho_g \vec{v}_g.E_g\right) = \nabla.(\lambda_g.\nabla T_s) + Q_{g,s} + S_{rad,g} + S_{rxn}$ (17)	
	Solid phase $\frac{\partial \alpha_s \rho_s E_s}{\partial t} + \nabla.\left(\alpha_g \rho_g \vec{v}_g.E_s\right) = \nabla.(\lambda_s.\nabla T_s) + Q_{g,s} + S_{rad,s}$	(18)
Radiative transfer equation (RTE)	$\nabla.(I.s) + (a_g + a_s + \sigma_s).I(r,s) = \{(1-\alpha_s).a_g + \alpha_s.a_s\}.\frac{\sigma\{(1-\alpha_s).T_g + \alpha_s.T_s\}^4}{\pi} + \frac{\sigma_s}{4.\pi}.\int_0^{4.\pi} I(r,s).\Phi_{isotropic}(s,s')d\Omega'$	(19)
Constitutive Equations		
Solid pressure	$p_s = 2.\rho_s.(1+e_{ss}).{\alpha_s}^2.g_{0,ss}.\theta_s$	(20)
Solid stress tensor	$\bar{\bar{\tau}}_s = \alpha_s.\mu_s.[(\nabla.\vec{v}_s + \nabla {v_s}^T)] + (\alpha_s.\lambda_s - \frac{2}{3}\alpha_s.\mu_s)\,\nabla.\vec{v}_s\bar{\bar{I}}$	(21)
Solid shear viscosity	$\mu_s = \mu_{s,kin} + \mu_{s,col}$	(22)
Kinetic viscosity	Gidaspow et al. (1992) $\mu_{s,col} = \frac{4}{5}.\alpha_s.\rho_s.d_s.g_{0,ss}(1+e_{ss})(\frac{\theta_s}{\pi})^{1/2}$ (23)	
Collisional viscosity	Syamlal et al. (1993) $\mu_{s,kin} = \frac{\alpha_s.d_s.\rho_s.\sqrt{\pi\theta_s}}{6.(3-e_{ss})}[1 + \frac{2}{5}.\alpha_s.g_{0,ss}(1+e_{ss})(3e_{ss}-1)]$ (24)	
Bulk viscosity	$\lambda_s = \frac{4}{3}.\alpha_s.\rho_s.g_{0,ss}.(1+e_{\ ss}).(\frac{\theta_s}{\pi})^{1/2}$	(25)

Radial distribution	$g_{0,ss} = [1 - \left({\alpha_s}/{\alpha_{s,max}}\right)^{1/3}]^{-1}$	(26)
Momentum exchange coefficient	Huilin et al. (2003) $\beta = \Psi.\beta_{Ergun} + (1-\Psi).\beta_{Wen\&Yu}$	(27)
	$\Psi = \frac{1}{2} + \frac{\arctan(262.5(\alpha_s - 0.2))}{\pi}$	(28)
	$\beta_{Ergun} = 150\frac{\mu_g.\alpha^2{}_s}{d^2{}_s.\alpha_g} + 1.75\frac{\alpha_s.\rho_g}{d_s}\lvert\vec{v}_s - \vec{v}_g\rvert$ *for* $\alpha_g \leq 0.8$	(29)
	$\beta_{Wen\&Yu} = \frac{3}{4}\frac{C_D.\alpha_s.\alpha_g.\rho_g}{d_s}\lvert\vec{v}_s - \vec{v}_g\rvert\alpha_g{}^{-2.65}$ *for* $\alpha_g > 0.8$	(30)
	$C_D\begin{cases}\frac{24}{\alpha_g.Re_s}[1 + 0.15.(\alpha_g.Re_s)^{0.687} & Re_s < 1000 \\ 0.44 & Re_s \geq 1000\end{cases}$	(31)
Granular temperature conductivity	Syamlal et al. (1993) $k_{\theta_s} = \frac{15\alpha_s.d_s.\rho_s.\sqrt{\pi\theta_s}}{4.(41-33\eta)}[1 + \frac{12}{5}.\eta^2.(4\eta-3)\alpha_s.g_{0,ss} +$ $\frac{16}{15\pi}(41-33\eta).\eta.\alpha_s.g_{0,ss}]$	(32)
	and $\eta = \frac{1}{2}.(1 + e_{ss})$	(33)
Energy collision dissipation	Gidaspow et al. (1992) $\varphi_{gs} = -3\beta\theta_s$	(34)
Interphase heat transfer	$Q_{s,g=}h_{s,g}(T_s - T_g)$	(35)
	With $h_{s,g} = \frac{6.\lambda_s\alpha_s.\alpha_g.Nu_s}{d_p^2}$	(36)
	Gunn (1978) $Nu_s = (7 - 10.\alpha_s + 5\alpha_s{}^2).\left(1 + 0.7Re_s{}^{0.2}.Pr^{1/3}\right) +$ $\left(1.33 - 2.4.\alpha_s + 1.2\alpha_s^2\right).Re_s{}^{0.7}.Pr^{1/3}$	(37)
Radiation source terms	Fluid phase: $S_{rad,g} = a_g.(\int_0^{4\pi} I.d\Omega - 4.\sigma T_g{}^4)$	(38)
	Gas phase: $S_{rad,s} = a_s.(\int_0^{4\pi} I.d\Omega - 4.\sigma T_s{}^4)$	(39)

The gas local absorptivity a_g in Eqs.6 and 19 was calculated as a function of the mass fraction of water vapor and carbon dioxide using the Fluent© WSGGM-Domain based model as these two gases are the most absorbing/emitting gases in the mixture and are considered to represent the overall radiation/gas phase interaction. The spouted particles radiation absorption and scattering coefficients (in Eq.19) were calculated by Eqs.40-41 with $Q_{ab,\lambda}$, $Q_{sc,\lambda}$ the efficiencies of absorption and scattering. As $d_s/\lambda >> 1$, the geometric regime can be applied and $Q_{ab,\lambda} = Q_{sc,\lambda} \sim 1$ (Bohren and Huffman, 2004). These equations were coupled to the Fluent© solver via a User Defined Function (UDF).

$$a_s = {3}/{2}.\alpha_s.{Q_{ab,\lambda}}/{d_s} \quad (40)$$

$$\sigma_s = {3}/{2}.\alpha_s.{Q_{sc,\lambda}}/{d_s} \quad (41)$$

In regions of high particles concentration, the diffusion becomes dependent on the distance between the particles. A method exists to introduce in the RTE corrected absorption and scattering efficiencies and phase function (Auger et al., 2000). This allows taking into account the effects of the near-field dependent scattering, which increases the accuracy of the predictions at the expense of the computational cost. In the current study and for the sake of simplification, these aspects were not taken into account in the modelling.

The variations in the fluid physical properties were considered, as the gas phase temperature varies from 25°C to more than 1200°C inside the reactor. The gas density was modeled by the ideal gas law and the kinetic theory was used to calculate intrinsic viscosities, thermal conductivities and mass diffusivities of each gas.

2.3 Numerical procedure

The commercial package Fluent© 19.1 was used. The Finite-Volume Method (FVM) was adopted and integral balance equations were formulated for each control volume. The transient conservation equations for both granular and gas phases were solved with a time step of 10^{-4}s for Eulerian-Eulerian approach. A time step of 10s was used for solving the energy equation for the solid components of the reactor (alumina cap, insulation, cavity walls). The reactor was first heated to a stationary temperature, then, the granular materials were patched into the fluid domain with an initial temperature of 1000°C. The phase coupled SIMPLE algorithm, which is an extension of the SIMPLE algorithm for multiphase flow, was used for the pressure–velocity coupling and correction. The momentum, volume fraction and energy equations were discretized by a first-order upwind scheme. A convergence criterion of 10^{-4} for each scaled residual component was specified for the relative error between two successive iterations for the continuity and the momentum equations. For the energy and radiation, a convergence criterion of 10^{-6} was used. The granular and gas phase average temperatures were also monitored for confirming the complete convergence, and should reach periodic and statistically constant values. Concerning the empty and the fixed bed configurations, the governing equations were solved in steady state with the coupled solver. Due to the low Re number inside the cavity, a laminar solver was selected for all the cases for solving the conservation equations.

3. Complementary results

3.1 Mass balance

The mass balance was checked systematically at the end of the experiments, Table.SI 3 presents the mass balance closure for the eleven runs.

Table SI 3. Mass balance (Runs#1-11)

Run#	Reactants (g)		Products (g)		Mass balance closure
	Biomass	H_2O	Gas products	Residues in outlet reactor components	
1	30.0	6.8	25.5	12.6	103.6%
2	30.0	6.8	26.9	8.3	93.3%
3	30.0	7.0	27.0	6.2	88.2%
4	30.0	6.8	24.6	7.3	86.8%
5	30.0	6.3	24.1	6.6	84.8%
6	30.0	7.7	26.8	5.9	86.8%
7	15.6	3.5	13.4	5.8	99.3%
8	30.0	6.7	27.4	7.7	95.6%
9	30.0	6.1	26.8	6.5	92.2%
10	30.0	6.7	26.8	7.8	94.3%
11	30.0	6.9	26.7	6.9	91.1%

3.2 Hydrodynamic simulations

A comparative study of the three configurations was carried out based on a purely hydrodynamic model (only momentum equations are solved). Accordingly, gas (mixture of Ar and steam, see section 2.1 for BCs, window flow rate set to 0 NL/min) physical properties (ρ, μ) were assumed constant and were calculated at a fixed temperature. The choice of this temperature is important as it affects the velocity that spouts the beds (due to gas expansion) which in turn strongly influences the gas-particles flow patterns (Olazar et al., 1992). In the studied configuration, the gas flow entered the injection tube at ambient temperature where it got heated before reaching the cone entrance. The achieved temperature near the cone entrance in the empty configuration was around 400°C (Boujjat et al. 2019). This value was used as rough estimate of the actual temperature at which the spouting takes place. Under these conditions, the inlet gas velocity was calculated by Eq.42.

$$V_{inlet,spouting} = {(\dot{m_{Ar}} + \dot{m}_{H_2O})_{exp}} \Big/ {\{(1 - x_{m,H_2O}).\rho_{Ar}(400°C) + x_{m,H_2O}.\rho_{H_2O}(400°C).S_{inlet\ tube}\}} \quad (42)$$

The predicted solid particles distributions for the spouted 10g bed particles (including SiC, Al_2O_3, olivine and sand) are shown in Figure.SI 4.

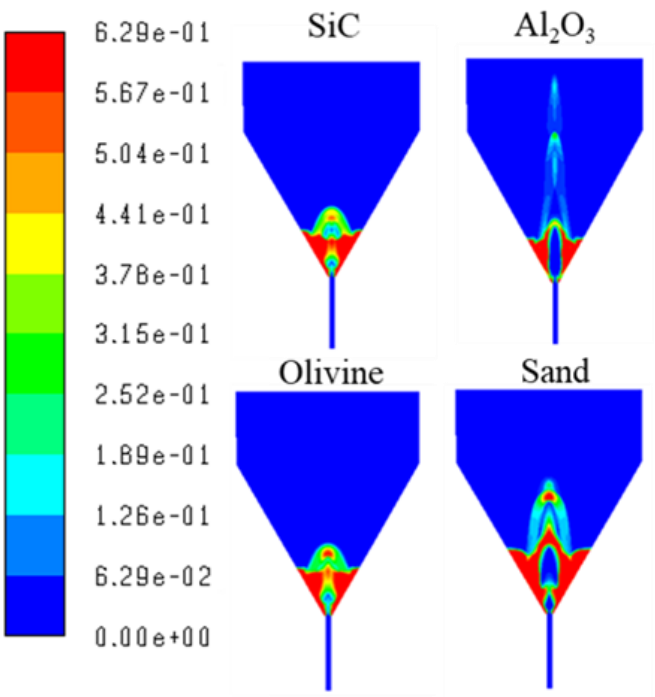

Figure SI 4. Inert particles space distribution at experimental conditions (t=2s), $V_{inlet,spout}$=6.91 m/s.

It was observed that the inlet gas flow rate was high enough to spout all the powders in a cyclic fashion without risk of entraining the finest ones (Al_2O_3 and sand) by the gas central jet stream. Moreover, for the SiC particles, the simulations pointed out that even if the inlet gas velocity was lower than the minimum spouting velocity measured during the cold tests, the spouting could still occur due to the increase in the gas kinematic viscosity. Furthermore, it was noted that the Al_2O_3 particles reached the highest degree of mixing with a fountain height that was three to four times the fountain height of the SiC and olivine particles while it roughly doubled the fountain height of the sand particles. Finally, as the olivine and SiC particles have very close characteristics (in terms of diameter and density); their solid flow patterns were almost identical.

The gas velocity magnitude was plotted in Figure.SI 5 at a horizontal plan (p) for the empty, the Al_2O_3 and SiC spouted beds, and for the Al_2O_3 packed bed. Globally, for the empty and the Al_2O_3 spouted bed, the curves had a bell-like shape with peak velocity values approaching 5m/s in the central region. The central gas velocities were significantly lower (~0.5 m/s) with the SiC particles that somehow diverted the flow towards the annular region due to their larger size. In the packed bed configuration, the gas velocity was more homogeneously distributed over plan (p) and was therefore the lowest (~0.05 m/s).

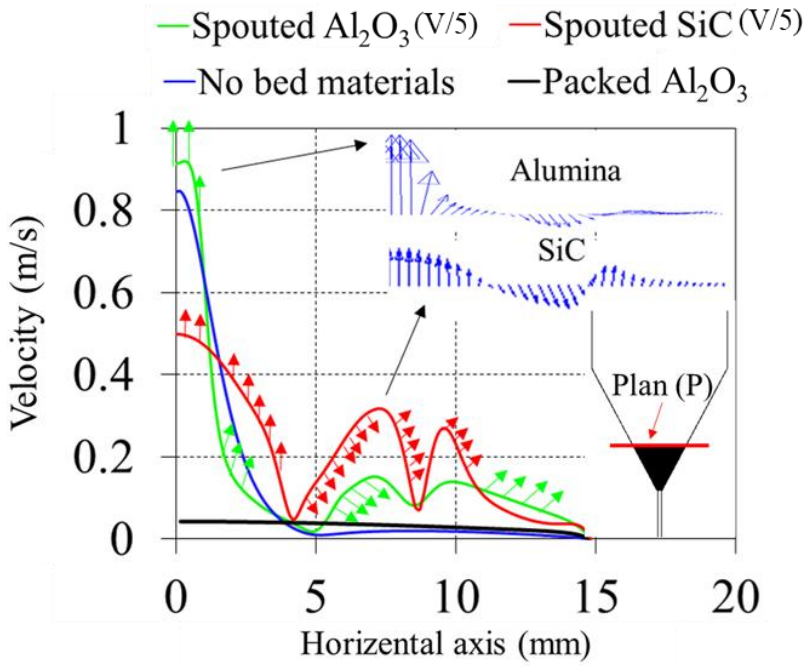

Figure SI 5. Gas velocity magnitude at a horizontal plan (plan (p)); (b) - Gas main pathlines colored by residence time

3.3 Char particles flow

To assess the trajectories of char particles inside the empty and the packed bed cavity, non-reacting particles were tracked for a few seconds using the discrete phase model (DPM) approach. The char particles characteristics were: d_{char}=0.35 mm, ρ_{char}=144 kg/m^3, $c_{p,char}$=1000 J/kg.°C. They were injected from the top of the reactor for the packed bed configuration and from the center of the gas jet for the empty configuration (Figure 6). A mass flow rate of 0.05 g/min of char was continuously injected. Figure 6-a shows the temperature of a tracked char parcel as function of time for the two hydrodynamic configurations and Figure 6-b shows the particles trajectories colored by particles velocity.

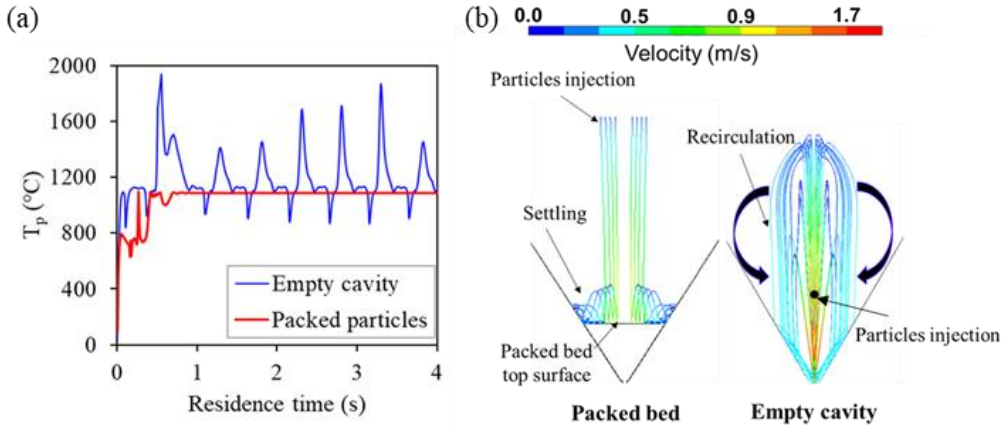

Figure SI 6. (a) DPM temperature, (b) DPM trajectories colored by particles velocity magnitude

For the empty case, the simulations predicted a fluctuating temperature pattern depending on the location of the particles in the reaction zone. In fact, the particles were entrained cyclically toward the source of radiation with a velocity of 1.7 m/s, and their temperature could thus reach crest values above 1500°C. When reverting to the bottom of the reactor due to gravity, they were cooled to 900°C by the inlet jet gases. On the contrary, in the packed bed configuration, the particles settled rapidly just after injection on the top of the bed. Their temperature was therefore constant at around 1150°C. This clearly confirms the interest of using the packed Al_2O_3 particles to limit the entrainment of the particles and broaden the inlet gas jet over the entire cavity surface.

4. References

Auger, J.C, Stout, B., Lafait, J., 2000. Dependent light scattering in dense heterogeneous media. Physica B 279, 21-24.

Bohren, C.F., Huffman, D.R., 2004. Absorption and Scattering of Light by Small Particles. Wiley-Vch, Weinheim

Boujjat, H., Rodat, S., Chuayboon, S., Abanades, S., 2019. Numerical simulation of reactive gas-particle flow in a solar jet spouted bed reactor for continuous biomass gasification. Int. J. Heat Mass Transf. 144, 118572.

Gelderbloom, S.J., Gidaspow, D., Lyczkowski, R.W, 2003. CFD simulations of bubbling/collapsing fluidized beds for three Geldart Groups. AIChE J. 49, 844– 858.

Gidaspow, D., Bezburuah, R., Ding, J., 1992. Hydrodynamics of circulating fluidized beds: Kinetic theory approach. Proceedings of the Seventh Engineering Foundation Conference on Fluidization.

Gore, R.A., Crowe, C.T., 1988. Observations on the flow in a confined coaxial jet. American Institute of Aeronautics and Astronautics 88-3591-CP.

Gunn, D.J., 1978. Transfer of heat or mass to particles in fixed and fluidized beds. Int. J. Heat Mass Transfer 21, 467–76.

Huilin, L., Gidaspow, D., 2003. Hydrodynamics of binary fluidization in a riser: CFD simulation using two granular temperatures. Chem. Eng. Sc. 58, 3777–3792.

Ismail, T-M., Abd El-Salam, M., Monteiro, E., Rouboa, A., 2018. Fluid dynamics model on fluidized bed gasifier using agro-industrial. Waste Management 73, 476-486.

Johnson, P.C., Jackson, R., 2006. Frictional–collisional constitutive relations for granular materials, with application to plane shearing. J. Fluid Mech. 176, 67–93.

Syamlal, M., Rogers, W., O'Brien, T.J., 1993. MFIX Documentation, Theory Guide, National Technical Information Service, Springfield.

Wang, J., 2008. High-resolution Eulerian simulation of RMS of solid volume fraction fluctuation and particle clustering characteristics in a CFB riser. Chem. Eng. Sci. 63, 3341–3347.

Olazar, M., San Jose, M.J., Aguayo, A.T., Arandes, J.M., Bilbao, J.; 1992. Stable operation conditions for gas-solid contact regimes in conical spouted beds. Ind. Eng. Chem. Res. 31, 1784–1792.